


Stability of nonminimally coupled topological-defect boson stars

Gray D. Reid  and Matthew W. Choptuik 

*Department of Physics and Astronomy, University of British Columbia,
Vancouver British Columbia, V6T 1Z1 Canada*

 (Received 21 August 2023; accepted 19 September 2023; published 4 January 2024)

As shown by Marunovic and Murkovic [*Classical Quantum Gravity* **31**, 045010 (2014)], nonminimal d-stars, composite structures consisting of a boson star and a global monopole nonminimally coupled to the general relativistic field, can have extremely high gravitational compactness. In a previous paper we demonstrated that these ground-state stationary solutions are sometimes additionally characterized by shells of bosonic matter located far from the center of symmetry [*Phys. Rev. D* **93**, 044022 (2016)]. In order to investigate the question of stability posed by Marunovic and Murkovic, we investigate the stability of several families of d-stars using both numerical simulations and linear perturbation theory. For all families investigated, we find that the most highly compact solutions, along with those solutions exhibiting shells of bosonic matter, are unstable to radial perturbations and are therefore poor candidates for astrophysically relevant black hole mimickers or other highly compact stable objects.

DOI: [10.1103/PhysRevD.109.024008](https://doi.org/10.1103/PhysRevD.109.024008)

I. BACKGROUND

Attempts to create stable solitonic solutions in the context of general relativity go back to Wheeler in 1955 with the development of geons—solitonic objects comprised of various fundamental fields coupled to gravity [1]. Although Wheeler’s geons proved to be unstable in general, further work by Kaup [2] and Ruffini and Bonazzola [3], lead to the discovery of the stable massive solitons today known as boson stars [4].

Over the intervening years, boson stars and their descendants have been invoked for a large variety of processes and models including black hole mimickers [5,6], models of neutron stars [5,7–10], binary systems [9], sources of dark matter [11–16] and sources of gravitational waves [9,11]. Though boson stars are not known to exist in nature, the simplicity of their matter model makes them a valuable tool for qualitative analysis and for providing a simple first step and test bed for more complex matter models [4,9].

Studies have demonstrated that boson stars are stable to perturbations provided that the central density of the star is sufficiently small [4,11,17–19]. However, without a self-interaction term in the potential, the mass of the star scales as $\frac{1}{2}m_p^2/m$ (where m_p is the Planck mass and m is the boson mass). For reasonable particle masses, this results in stars with masses far below the usual Chandrasekhar limit for fluid stars [4,20,21]. Thus, these so-called mini-boson stars are useful primarily as a test bed with their more specialized cousins (having, for example, additional terms in the potential) being adapted to various astrophysical situations [4].

Whereas boson stars gain their stability through a conserved charge and the interplay between pressure and gravity, global monopoles are topologically stable [22–24]. Along with other topological defects such as textures, domain walls, and strings, monopoles are expected to form fairly generically when underlying field symmetries are broken through early universe phase transitions which are mediated by expansion and cooling [24].

In the case of the monopole, the simplest class of defect consists of a scalar field triplet with a global $O(3)$ symmetry which is spontaneously broken to $U(1)$ on a noncontractible 2-surface. If the broken symmetry is local, the resulting monopole is shielded by the Maxwell field and has finite energy and extent. Conversely, if the field exhibits a global symmetry, we find that the resulting energy is linearly divergent in radius [22–25].

Although this divergence may seem somewhat problematic, there are two important caveats. First, the energy divergence cuts off upon encountering another monopole or antimonopole. Second, in the context of general relativity, the energy divergence has the simple effect of producing a solid angle deficit spacetime along with a small effective negative mass core, rather than more exotic features [22,23,25,26]. As shown by Barriola *et al.* [22], we would expect global monopoles and anti-monopoles to annihilate extremely efficiently due to the fact that the interaction strength between them is independent of distance. Although this annihilation is avoided by local monopoles, we expect a Hubble volume to contain only ≈ 1 global monopole at the present time due to the efficiency of this interaction.

Putting aside these considerations, when a global monopole and boson star are combined, the result is a novel object referred to as a topological-defect boson star or “d-star.” Previously studied in [5,26–28], it was shown that through nonminimal coupling and proper choice of interaction parameters, d-stars could be made extremely dense, thereby potentially acting as mimickers of black holes or other highly compact objects [5]. Subsequent in-depth investigation of these objects revealed novel interactions and ground state solutions [26]. When viewed as functions of the boson star central density, these ground state solutions are characterized by discontinuous changes in the global properties of the system (mass, charge, etc.). To better describe this behavior, we borrow the terminology of statistical mechanics. In this analogy, the central density of the boson star takes the place of the temperature, the asymptotic mass takes the role of the energy and the mass gap is similar to latent heat.

The discontinuous changes in global properties are mediated by the appearance or disappearance of shells of bosonic matter at characteristic radii which can be either finite or infinite. We use the term asymptotic shell to refer to any shell of matter which first appears far from the coordinate origin as $\psi(0)$ is increased past some critical value and which subsequently vanishes when $\psi(0)$ is further increased past a second critical value. We refer to those families of solutions with mass gaps (when the mass is viewed as a function of the central density) as expressing a first order phase transition. Those with discontinuities in the derivative of the asymptotic mass or charge express a second order phase transition. The interested reader is directed to [26] for an in-depth review.

II. REVIEW OF STATIONARY D-STARS

We have previously solved the equations of motion assuming stationary solutions, the harmonic ansatz for the boson field and a hedgehog ansatz for the monopole fields [26]. The solutions we discovered were characterized by a series of discrete boson star central amplitudes, $\psi_i^c(0)$, about which the character of the solutions changed discontinuously in a manner analogous to a phase transition. In what follows, we will use the same terminology and notation as our previous paper [26], which is briefly reviewed below.

The parameter space we consider here is six-dimensional, spanned by the central amplitude of the boson star, $\psi(0)$, and five coupling parameters: the solid angle defect, Δ^2 , the quartic global monopole potential parameter, λ_G , the quartic boson star potential parameter, λ_B , the global monopole nonminimal coupling, ξ_G , and the boson star nonminimal coupling, ξ_B . We fix the mass of the boson star field, $m = 1$, and note that this sets the energy scale of the solutions. We define a family of solutions to be the set of all ground state solutions with common $\Delta, \lambda_G, \lambda_B, \xi_G$ and ξ_B . As such, within a given family, solutions can be indexed by the boson star

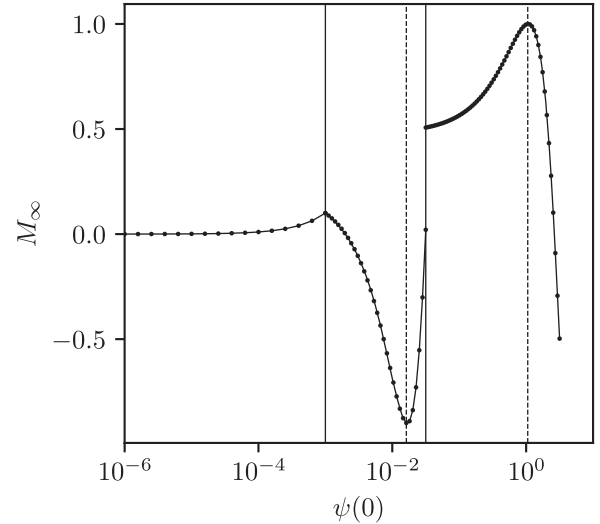


FIG. 1. Asymptotic mass as a function of central amplitude for a hypothetical family consisting of three branches. The first branch consists of a single region while each of the subsequent branches consist of two regions, the extent of which are delimited by their mass turning points. Solid vertical lines denote the extent of branches while regions within a branch are separated with vertical dashed lines.

central amplitude, $\psi(0)$, which is the only free parameter of the family (see Fig. 1).

Due to the large parameter space associated with these solutions, it was not feasible to perform a comprehensive parameter space survey. Instead, as in [26], we focus on a number of families of solutions which appear to capture the novel behavior associated with the model. In subsequent sections we deal with eight families of solutions whose fixed parameters are given in Table I. For simplicity, the boson star quartic self interaction coupling constant, λ_B , has been set to 0 under the assumption that its primary effect will be to produce more compact objects (while having

TABLE I. Families of solutions and their associated parameters. Each family consists of a continuum of solutions labeled by the central amplitude of the boson star. In particular, family h corresponds to a family in the high compactness regime as defined in [5]. Due to their relatively simple and illustrative modal structure, families p_1 and p_2 are the only ones we explore with perturbation theory.

Family	Δ^2	λ_B	λ_G	ξ_B	ξ_G
c	0.36	0	1.000	0	0
d	0.81	0	0.010	0	0
e	0.25	0	0.001	3	3
f	0.49	0	0.010	5	0
g	0.09	0	0.010	0	5
h	0.08	0	0.100	-4	5
p_1	0.09	0	0.040	0	0
p_2	0.25	0	0.040	0	0

only a minor effect on the low density asymptotic shells that we find). Those families that were investigated in [26] were given identical designations.

We define a *branch* of a family to be the set of all solutions in the family where the asymptotic mass, M_∞ , is C^1 as a function of the central amplitude, $\psi(0)$. Using this definition, Fig. 1 provides a mass plot illustrating a hypothetical family with three branches. We use the term *region* to refer to the set of all solutions on a given branch between extremal values of the asymptotic mass. Using our previous example, the first branch of Fig. 1 consists of a single region while the second and third branches each consist of two regions.

As demonstrated in Fig. 2, which plots the asymptotic mass, M_∞ , of a family of solutions, this mass parameter is not in general a smooth function of the boson star central amplitude, $\psi(0)$, as would be expected for a fluid star. As we construct families of stationary solutions by varying the central amplitude of the boson star (keeping all other parameters fixed) we find that when the central amplitude is increased or decreased across a critical point $\psi_i^c(0)$, a shell of bosonic matter will either appear or vanish far from the center of symmetry. As shown in [26], these shells of matter may either appear suddenly at spatial infinity, or gradually at a finite radius when the boson star is non-minimally coupled to gravity.

As discussed in full detail in [26], these families of solutions have features that are in many ways analogous to critical points and phase transitions in thermodynamical systems. When shells appear at infinity with finite mass, we

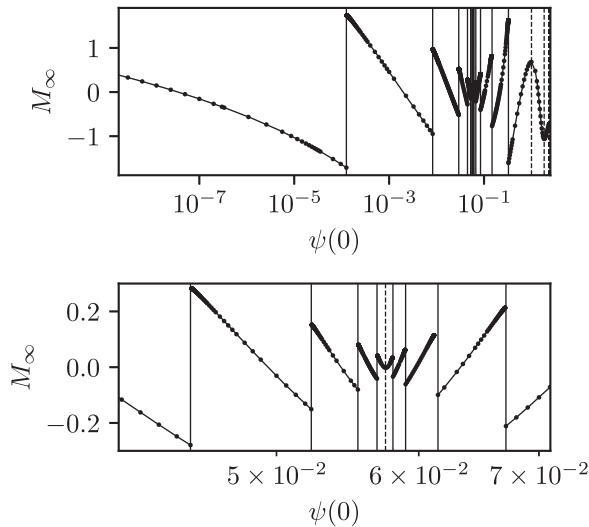


FIG. 2. Asymptotic mass as a function of central amplitude for family d . The lower panel shows an expanded view of the upper plot highlighting the central structure. As demonstrated in [26], the apparent discontinuities are genuine. These discontinuities correspond to shells of bosonic matter of finite mass and particle number appearing or disappearing at spatial infinity.

have a direct analogy with first order phase transitions with $\psi(0)$ taking the role of the temperature or pressure and the mass gap being analogous to the latent heat. When the transition is gradual, as in the case of nonminimal coupling, we have a situation more analogous to second order, or continuous, phase transitions.

III. OVERVIEW

In analyzing the stability of the boson d-star solutions, we adopt a two pronged approach. First, we consider the general nonminimally coupled case and perform dynamical simulations of a number of families which seem to be representative of the model as a whole. Specifically, from these families we choose a few solutions from each branch, perturb the solutions and follow the evolution of the system, looking for growth of excited modes. Previous studies have shown that stability transitions are confined to turning points of the asymptotic mass or charge when these quantities are viewed as functions of boson star central amplitude [17–19,29]. We greatly simplify our investigation by considering only a small number of evolutions per region and by assuming that the observed stability for these simulations generalizes across the entire region.

Our second approach involves a detailed analysis of the mode structure of the d-star solutions via linear perturbation analysis. Due to the complexity of the resulting equations for the nonminimally coupled case, we limit ourselves to the investigation of the minimally coupled configurations. Through an exhaustive investigation of two families, we deduce a general mode structure which is in broad agreement with the results of our dynamical simulations.

IV. MATTER MODEL

Following the prescription of Marunovic and Murkovic [5], the dimensionless Einstein-Hilbert action ($c = 1$, $G = 1/8\pi$) is given by

$$S_{\text{EH}} = \int dx^4 \sqrt{-g} \frac{R}{2} \quad (1)$$

while the actions for the boson star and global monopole are

$$S_B = \int dx^4 \sqrt{-g} \left[-\frac{1}{2} (\nabla_\mu \Psi^*) (\nabla^\mu \Psi) - V_B + \frac{\xi_B}{2} R (\Psi^* \Psi) \right], \quad (2)$$

$$S_G = \int dx^4 \sqrt{-g} \left[-\frac{\Delta^2}{2} (\nabla_\mu \phi^a) (\nabla^\mu \phi^a) - V_G + \frac{\xi_G}{2} R \Delta^2 (\phi^a \phi^a) \right]. \quad (3)$$

Here, Ψ is the complex boson star field, ϕ^a are scalar field triplets comprising the monopole, V_B and V_G are the self interaction potentials for the boson field and monopole fields respectively, R is the Ricci scalar and ξ_B and ξ_G are the nonminimal coupling constants. The stress-energy tensors associated with the matter actions are

$$T_{\mu\nu}^B = \frac{1}{2} \nabla_\mu \Psi^* \nabla_\nu \Psi + \frac{1}{2} \nabla_\nu \Psi^* \nabla_\mu \Psi - \frac{1}{2} g_{\mu\nu} (\nabla_\alpha \Psi \nabla^\alpha \Psi^* + 2V_B) - \xi_B (G_{\mu\nu} + g_{\mu\nu} \nabla_\alpha \nabla^\alpha - \nabla_\mu \nabla_\nu) \Psi \Psi^*, \quad (4)$$

$$T_{\mu\nu}^G = \frac{\Delta^2}{2} \nabla_\mu \phi^a \nabla_\nu \phi^a + \frac{\Delta^2}{2} \nabla_\nu \phi^a \nabla_\mu \phi^a - \frac{1}{2} g_{\mu\nu} (\Delta^2 \nabla_\alpha \phi^a \nabla^\alpha \phi^a + 2V_G) - \xi_G \Delta^2 (G_{\mu\nu} + g_{\mu\nu} \nabla_\alpha \nabla^\alpha - \nabla_\mu \nabla_\nu) \phi^a \phi^a. \quad (5)$$

We use the standard 3+1 decomposition where 4D spacetime is foliated into a sequence of spacelike hypersurfaces, Σ_t , such that each hypersurface of constant t has a 3-metric, γ_{ij} . Explicitly, the 4-metric takes the form

$$g_{\mu\nu} = \begin{pmatrix} -\alpha^2 + \beta^i \beta_i & \beta_j \\ \beta_i & \gamma_{ij} \end{pmatrix}. \quad (6)$$

with a timelike normal, n^ν , to the foliation, Σ_t , given by

$$n^\nu = \left(\frac{1}{\alpha}, -\frac{\beta^i}{\alpha} \right). \quad (7)$$

Here, α and β^i are the usual lapse and shift respectively. We impose spherical symmetry, and adopt polar-areal coordinates such that the line element becomes

$$ds^2 = -\alpha(t, r)^2 dt^2 + a(t, r)^2 dr^2 + r^2 (d\theta^2 + \sin^2 \theta d\phi^2). \quad (8)$$

Decomposing the boson field into a real and imaginary part and taking the hedgehog ansatz for the monopole, the matter fields and corresponding potentials are

$$\Psi = \phi_R + i\phi_I, \quad (9)$$

$$\phi^a = \phi_M \frac{x^a}{r}, \quad (10)$$

$$V_G = \frac{\lambda_G}{4} \Delta^4 (\phi_M^2 - 1)^2, \quad (11)$$

$$V_B = \frac{m^2}{2} (\phi_R^2 + \phi_I^2) + \frac{\lambda_B}{4} (\phi_R^2 + \phi_I^2)^2. \quad (12)$$

Varying the actions with respect to the matter fields gives the equations of motion for the matter:

$$\nabla_\mu \nabla^\mu \phi_R = \phi_R \partial V_{\phi_R} - \xi_B R \phi_R, \quad (13)$$

$$\nabla_\mu \nabla^\mu \phi_I = \phi_I \partial V_{\phi_I} - \xi_B R \phi_I, \quad (14)$$

$$\nabla_\mu \nabla^\mu \phi_M = \frac{\phi \partial V_{\phi_M}}{\Delta} + \frac{2\phi_M}{r^2} - \xi_G R \phi_M, \quad (15)$$

where:

$$\partial V_{\phi_R} = m^2 \phi_R + \lambda_B (\phi_R^2 + \phi_I^2) \phi_R, \quad (16)$$

$$\partial V_{\phi_I} = m^2 \phi_I + \lambda_B (\phi_R^2 + \phi_I^2) \phi_I, \quad (17)$$

$$\partial V_{\phi_M} = \lambda_G \Delta^4 (\phi_M^2 - 1) \phi_M. \quad (18)$$

We express the fields $\phi_A = (\phi_R, \phi_I, \phi_M)$ in terms of their conjugate momentum and spatial derivatives:

$$\Pi_A = \frac{a}{\alpha} \partial_t \phi_A \quad (19)$$

$$\Phi_A = \partial_r \phi_A \quad (20)$$

Evaluating tensor components and simplifying, the equations of motion for the matter fields may be expressed as

$$\partial_t \Pi_R = -(\xi_B \phi_R T + \partial_{\phi_R} V) \alpha a + \partial_r \left(\frac{\Phi_R \alpha}{a} \right) + \frac{2\Phi_R \alpha}{ra}, \quad (21)$$

$$\partial_t \Pi_I = -(\xi_B \phi_I T + \partial_{\phi_I} V) \alpha a + \partial_r \left(\frac{\Phi_I \alpha}{a} \right) + \frac{2\Phi_I \alpha}{ra}, \quad (22)$$

$$\partial_t \Pi_M = -\left(\xi_G \phi_M T + \frac{\partial_{\phi_M} V}{\Delta^2} + \frac{2\phi_M}{r^2} \right) \alpha a + \partial_r \left(\frac{\Phi_M \alpha}{a} \right) + \frac{2\Phi_M \alpha}{ar}. \quad (23)$$

$$\partial_t \Pi_P = \partial_r \left(\frac{\Phi_P \alpha}{a} \right) + \frac{2\Phi_P \alpha}{ra}. \quad (24)$$

Here, we have used the contracted Einstein equation $R = -T$, and have incorporated a massless scalar field, ϕ_P , to facilitate perturbation of the stationary solutions. The choice of polar-areal coordinates greatly simplifies the Einstein equations and after a considerable amount of manipulation we arrive at the form of the equations given in Appendix A.

A. Boundary conditions

Given the hedgehog ansatz (10), ϕ_M is the magnitude of the global monopole fields, ϕ^a , which are analogous to an outward pointing vector field. As such, to maintain regularity we must have $\phi_M = 0$, at the center of symmetry. Further, as $r \rightarrow 0$, regularity requires $\phi_R, \phi_I, \phi_P, \Pi_R, \Pi_I,$

Π_P , a , and α be even functions of r (with $a(t, 0) = 1$) while ϕ_M and Π_M are odd functions of r .

In the limit that $r \rightarrow \infty$, the boson star field exponentially approaches zero while the global monopole transitions to its vacuum state ($\phi_R \rightarrow 0$, $\phi_I \rightarrow 0$, $\phi_M \rightarrow 1 + \sum_i c_i r^{-i}$). Defining $\tilde{\Delta}$ by

$$\tilde{\Delta} = \frac{\Delta^2}{1 + \xi_G \Delta^2}, \quad (25)$$

and assuming a series expansion in $1/r$, the metric equations can be integrated to yield the following regularity conditions as r approaches infinity [5,13]:

$$\phi_R = \phi_I = \phi_P = 0, \quad (26)$$

$$\phi_M = 1 - \frac{1}{\lambda_G \Delta^2 r^2 (1 + \xi_G \Delta^2)}, \quad (27)$$

$$\Pi_R = \Pi_I = \Pi_P = \Pi_M = 0, \quad (28)$$

$$a = \left(1 - \tilde{\Delta} - \frac{2M}{r}\right)^{-1/2}, \quad (29)$$

$$\alpha = \left(1 - \tilde{\Delta} - \frac{2M}{r}\right)^{1/2}. \quad (30)$$

Here, M is a constant of integration proportional to the ADM mass of a solid angle deficit spacetime as defined in the next section.

B. Conserved and diagnostic quantities

The global $U(1)$ invariance of the boson star field gives rise to a conserved current,

$$\begin{aligned} J_\mu &= \frac{i}{16\pi} (\Psi^* \nabla_\mu \Psi - \Psi \nabla_\mu \Psi^*), \\ &= \frac{1}{8\pi} (\phi_I \nabla_\mu \phi_R - \phi_R \nabla_\mu \phi_I), \end{aligned} \quad (31)$$

with temporal component,

$$J_t = \frac{\alpha}{8\pi a} (\phi_I \Pi_R - \phi_R \Pi_I). \quad (32)$$

Associated with the current is a conserved charge,

$$N = \int J_\nu n^\nu \sqrt{\gamma} dx^3, \quad (33)$$

with spatial gradient,

$$\partial_r N = \frac{r^2}{2} (\phi_I \Pi_R - \phi_R \Pi_I). \quad (34)$$

Although the energy of the spacetime is linearly divergent in r , it is possible to use the prescription of Nucamendi *et al.* [25] to define an ADM-like mass, M_{ADM} , for a solid angle deficit spacetime as

$$\begin{aligned} M_{\text{ADM}} &= \frac{1}{16\pi(1 - \tilde{\Delta})} \int_{\partial\Sigma_t} (\bar{\gamma}^{ac} \bar{\gamma}^{bd} - \bar{\gamma}^{ab} \bar{\gamma}^{cd}) \\ &\quad \cdot \bar{D}_b(\gamma_{cd}) dS_a. \end{aligned} \quad (35)$$

Here $\bar{\gamma}_{ab}$ is a metric which is flat everywhere save a deficit solid angle, and which is induced on all constant time hypersurfaces, Σ_t . \bar{D}_b is the associated connection and dS_a is the surface area element [25].

Evaluation of (35) using the asymptotic forms of the metric functions (29)–(30) under the coordinate changes prescribed by Nucamendi, yields

$$M_{\text{ADM}} = M(1 - \tilde{\Delta})^{-3/2}, \quad (36)$$

where M is defined as in (29). We further define a mass function as

$$M(t, r) = \frac{r}{2} (1 - a(t, r)^{-2} - \tilde{\Delta}), \quad (37)$$

$$M_\infty \equiv \lim_{r \rightarrow \infty} M(t, r), \quad (38)$$

and use it to monitor energy conservation of the system. We also use the above definition of $M(t, r)$ to define a measure of the compactness of the system. Specifically, following Marunovic and Murkovic [5], we define the compactness as

$$C(t, r) \equiv \frac{2M(t, r)}{r(1 - \tilde{\Delta})}, \quad (39)$$

such that $C(t, r_0) \rightarrow 1$ indicates the development of an apparent horizon at areal radius r_0 . Correspondingly, we define the quantity C_{max} as

$$C_{\text{max}} \equiv \max(C(t, r)). \quad (40)$$

For any given configuration of matter, then, C_{max} measures the maximum compactness of the configuration.

V. DYNAMICAL SIMULATION

This section provides an overview of our evolution scheme and associated numerics. Section VA details the initialization of the metric and matter fields, while Sec. VB introduces the finite difference discretizations used to solve the equations of motion and describes the evolution procedure. Section VC specifies the tests used to ensure

convergence of our scheme. Finally, Sec. V D describes our method of extracting stable and unstable perturbative modes from the dynamical simulations.

A. Initial data

To initialize an evolution, the boson star fields, ϕ_R and ϕ_I , global monopole field, ϕ_M , and metric fields, a and α , are interpolated to the evolution grid from a stationary solution (computed using the methodology described in [26]) using a high order interpolation scheme. Subsequently, we add a small perturbation consisting of either a Gaussian pulse in the massless scalar field, ϕ_P , or a rescaling of the matter fields. Finally, the Hamiltonian and momentum constraints are re-integrated to account for the perturbation and the system is ready for evolution.

Specifically, when considering a case where the excited modes are observed to grow slowly compared to the light-crossing time of the star, the perturbation is set using a time-symmetric massless scalar field pulse of the form

$$\phi_P(0, r) = a_0 \exp\left(-\frac{(r - r_0)^2}{\sigma_0^2}\right), \quad (41)$$

where a_0 , σ_0 , and r_0 determine the location and intensity of the pulse at $t = 0$. A portion of this time symmetric pulse implodes inward and excites perturbative modes in the boson d-star before dispersing to infinity.

When the growth rate of the perturbative modes are large compared to the scale of the star, this approach fails to produce good results (e.g. the perturbations evolve into the nonlinear regime before the perturbing pulse is able to disperse). In this case, the truncation error induced by restricting the stationary solutions to the evolution grid (which is quite coarse compared to the one used to determine the time-independent solutions) induces growth modes over which we have very little control. These modes quickly become the dominant source of perturbation and hamper the extraction of useful information from the simulations. To overcome this, we introduce a perturbation by rescaling the matter fields as,

$$\phi_i(x) \rightarrow \phi_i((1 + \lambda)x), \quad (42)$$

where λ is taken to be a small number, typically on the order of 10^{-5} , and reintegrating the Hamiltonian and polar slicing condition. Here, x , is a compactified spatial coordinate as will be discussed shortly. Although this form of perturbation works well, it is decidedly less natural than perturbing with an external matter field and we stick to the former approach whenever possible.

B. Evolution scheme

We evolve the matter field quantities using (19)–(24) and a second order finite difference scheme with Crank-Nicholson

differencing. To damp high frequency solution components we add fourth order, temporally centered, Kreiss-Oliger dissipation. Due to the global nature of the monopole field, the need to evolve the simulations for many dynamical timescales, and the fact that it helps in implementing the $r \rightarrow \infty$ boundary conditions, we adopt compactified coordinates defined by:

$$r = \frac{\lambda x}{1 - x}, \quad 0 \leq x \leq 1, \quad (43)$$

where λ is a positive real number that typically satisfies $1 \leq \lambda \leq 100$. Specifically, λ is chosen so that all solution features are well resolved with our choice of mesh spacing. Since x compactifies the entire domain of r , this coordinate change works in conjunction with our numeric dissipation operators to suppress wave like oscillations far from $r = 0$. This in turn permits us to forgo crafting outgoing boundary conditions for our fields and instead impose trivial boundary conditions corresponding to (26)–(30) at the $x = 1$ limit of our domain. Care must be taken, however, to ensure that the parity of functions at the origin is treated according to their behavior in r rather than x .

As noted in Appendix A, it is possible to find an expression for $\partial_r a$ independent of α . As such, we may consider the equation for the metric as two initial value problems rather than a coupled boundary value problem. In practice, we find the most effective method of solving for the metric functions is to integrate $\partial_r a$ from $x = 0$ to $x = 1$, initialize $\alpha = 1/a$ at $x = 1$, and integrate $\partial_r \alpha$ back to $x = 0$.

Although our overall evolution scheme is well suited to the evolution of highly dynamical simulations, its utility for investigating nearly stationary solutions and the growth of perturbations is limited by the use of second order finite difference operators. In particular, there are significant restrictions on the period of time for which a simulation may be run before dispersion becomes the dominant factor limiting solution accuracy. The scheme was chosen for ease of implementation, but fourth order finite difference or spectral schemes would be far superior for the purpose of resolving modes with very slow growth rates.

C. Convergence

To validate the stability of the evolution scheme and to ensure that mass and charge are approximately conserved for dynamic configurations, we choose initial data consisting of a stationary solution perturbed by a large-amplitude massless scalar field pulse at the origin. The mass energy of the massless scalar field is a significant fraction of the total mass energy of the system, so the system as a whole is highly perturbed from stationarity. Specifically, the monopole is nonstationary far from the origin due to its coupling to the modified metric functions.

We demonstrate the convergence of our algorithm via the evolution of slightly subcritical (i.e. slightly stronger initial

perturbations would result in black hole formation), non-minimally coupled, initial data. In verifying the validity of our evolutionary scheme, we make use of the technique of independent residual evaluators. This involves creating alternative discretizations of the equations of motion (EOM) which are then applied to solutions computed via our evolutionary scheme. More explicitly, our evolutionary scheme solves the difference equations,

$$\tilde{D}(u^h) - f^h = 0, \quad (44)$$

where \tilde{D} is some nonlinear difference operator and u^h and f^h are our discretized fields with grid spacing h . The technique of independent residual evaluation involves finding an alternative discretization, \tilde{D}' , application of which to our precomputed solution, u^h , yields,

$$\tilde{D}'(u^h) - f^h = \tilde{r}^h. \quad (45)$$

If \tilde{r}^h is observed to converge at order $O(h^2)$, it implies that both \tilde{D} and \tilde{D}' match to order $O(h^2)$ and provides confidence—far beyond what can be achieved with standard convergence tests—that we are solving the correct EOM. Figure 3 shows representative independent residual convergence of strong field initial data for a range of grid spacings while Figs. 4 and 5 plot conserved quantity violations for the same solutions. From these plots, it can be seen that the solution algorithm is convergent in the strong field limit.

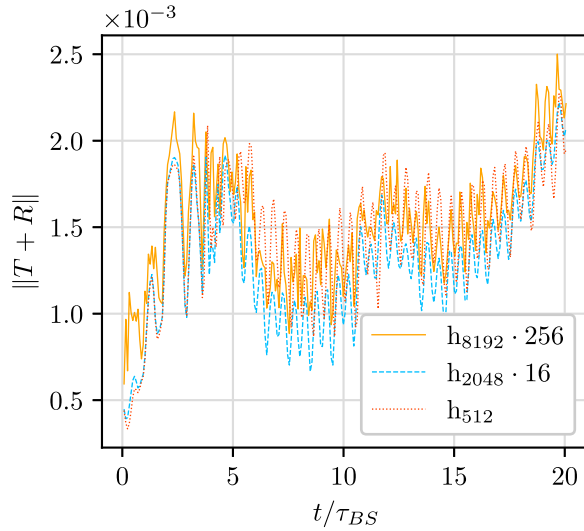


FIG. 3. Convergence of the l_2 -norm of independent residuals for the trace of the Einstein field equations ($T + R = 0$) in the case of a very strongly perturbed d-star. The residuals of the higher resolution simulations are scaled by 16 and 256, respectively such that overlap of the curves implies second order convergence. This figure encompasses approximately 50 light-crossing times or 20 periods of the central boson star oscillation, τ_{BS} .

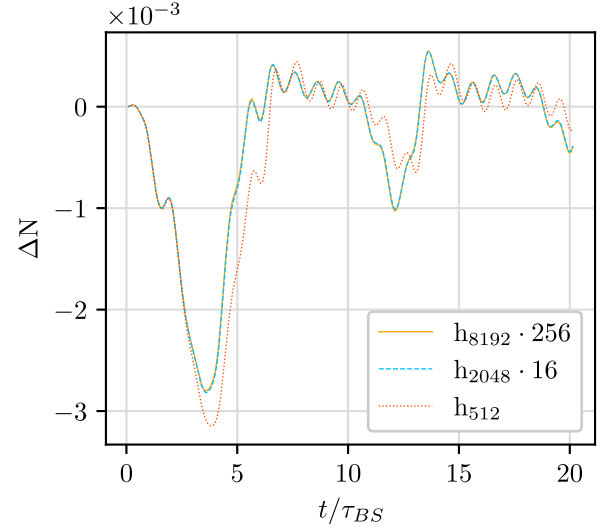


FIG. 4. Convergence of charge conservation for strong field data where the residuals of the higher resolution simulations have been scaled such that overlap of the curves implies second order convergence. The oscillation period of the unperturbed central boson star is denoted τ_{BS} .

D. Extraction of growth modes

The basic mechanics of a perturbation theory analysis suggest an obvious means by which the stability of a solution may be tested. By monitoring the growth rate of a quantity which would remain constant were the solution unperturbed, we can make a direct measurement of the eigenvalue of the dominant mode. In the case of instability, we expect to see exponential growth in the norm of the perturbation. In contrast, the norm of a perturbed quantity

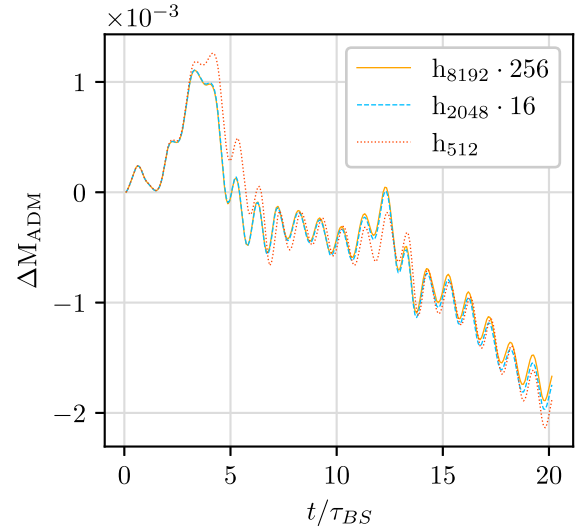


FIG. 5. Convergence of mass conservation for strong field data where the residuals of the higher resolution simulations have been scaled such that overlap of the curves implies second order convergence.

which is stable should oscillate in time. In both cases, the growth rate or period, respectively, may be determined by appropriate fits to the perturbed quantity.

A note of caution is, however, warranted: the method described above is only capable of determining a *lower* bound for the instability of the system. It is entirely possible for this method to miss unstable modes with eigenvalues much smaller than those of the excited stable modes (in which case the growth rate of the former is masked by oscillations of the latter). In an effort to counter this problem, we evolve the perturbed solutions for many dynamical timescales as given by the lowest frequency stable mode. This typically translates to hundreds of light-crossing times and thousands of boson star oscillations. Although we can never state with absolutely certainty that a solution is stable, we will nonetheless use that terminology when no growing modes are detected over such timescales.

Previous stability studies [17–19,29] have shown that boson stars, like fluid stars, undergo stability transitions only at solutions corresponding to extrema of the asymptotic mass, M_∞ , as is predicted by catastrophe theory. We therefore work under the assumption that all sets of stationary solutions in the same region (bounded by extrema of M_∞) exhibit similar stability properties. The results of Sec. VII B serve to validate this assumption for the minimally coupled case. The results presented in Sec. VII A are therefore derived from a small number of simulations chosen to be representative of each region in a given family. Typically, we perform between two and three simulations for each region.

In our analysis we make extensive use of the Noether charge as a stability diagnostic rather than using matter fields or metric functions. Given (33), we see that the Noether charge is a derived quantity, tied tightly to both the metric functions and bosonic matter fields. As such, any changes to those fields are immediately reflected in the Noether charge, making it an ideal quantity for monitoring stability and for comparing the form of excited modes to those predicted by perturbation theory.

VI. LINEAR PERTURBATION THEORY

Proceeding in standard fashion, we decompose the perturbed solution, $f(t, r)$, into a stationary component and an integral over Fourier modes:

$$f(t, r) = f_0(r) + \int_{-\infty}^{\infty} \hat{f}(r, \beta) e^{i\beta t} d\beta. \quad (46)$$

We substitute $f(t, r) = f_0(r) + \epsilon \delta f(r) e^{i\beta t}$ into the equations of motion and expand to linear order in ϵ . By doing so, we reduce our system of PDEs to a system of ODEs that represents the growth rate of various modes and that constitutes an eigenvalue problem in β^2 . In general, this system cannot be solved for all values of β^2 while retaining conservation of our conserved quantities; for most values of

β^2 , the solution obtained implies that the integral of the various conserved quantities is time dependent. For those countable number of modes that do satisfy the requisite boundary conditions for the conserved quantities, those with $\beta^2 > 0$ will be stable while those with $\beta^2 < 0$ will be unstable.

Following Gleiser and Watkins [18], we transform to a set of variables $(\mu(t, r), \nu(t, r), \psi_R(t, r), \psi_I(t, r), \phi(t, r))$ defined by:

$$a = e^{\mu/2}, \quad (47)$$

$$\alpha = e^{\nu/2}, \quad (48)$$

$$\Psi = e^{-i\omega t}(\psi_R + i\psi_I), \quad (49)$$

$$\phi_M = \phi. \quad (50)$$

The derivation and final form of the perturbation equations have been relegated to Appendix B due to their significant complexity.

A. Solution procedure

Even in the minimally coupled case, finding solutions to (B13)–(B18) proves to be quite challenging. Examination of the regularity conditions at the origin reveals that the appropriate degrees of freedom in the problem are given by β^2 , $\delta\psi_R(r)|_{r=0}$, $\delta\psi_I(r)|_{r=0}$ and $\partial_r\delta\phi(r)|_{r=0}$. Due to the linearity of the problem, we are free to set $\delta\psi_R(r)|_{r=0} = 1$ and the equations therefore constitute an eigenvalue-boundary value problem in the remaining degrees of freedom. In general, for inexactly chosen boundary values and β^2 , the matter and metric functions may only be integrated to a finite distance from the origin before the solution becomes pathological. As such, we cannot use, for example, gradient descent techniques to tune these parameters and instead turn to an iterative shooting method [26].

We expect that each successive mode of solutions to (B13)–(B18) will develop an additional node in each of the field variables. Correspondingly, we choose a trial value of β^2 (manually due to the difficulty encountered automating the process) and set $\delta\phi(r) = 0$. Once the fields have been initialized, we shoot on $\delta\psi_I(r)|_{r=0}$ for $\delta\psi_R$ and $\delta\psi_I$ holding $\delta\phi$ fixed until the bosonic fields are well behaved far from the origin. We then fit a decaying tail to $\delta\psi_R$ and $\delta\psi_I$, and shoot on $\partial_r(\delta\phi)|_{r=0}$ holding the bosonic fields fixed. This shooting procedure is repeated several times until approximate convergence is achieved. Finally, we examine δN_∞ and adjust β^2 , repeating the entire shooting procedure until a solution is found with $\delta N_\infty \approx 0$ to within tolerance (typically 0.05 of the maximum value of $\delta N(r)$ is sufficient). This process of determining initial data in compactified coordinates x is summarized in Algorithm 1.

Upon achieving the desired tolerance, the approximate solution is used as an initial guess for a boundary value problem solver based on the collocation library TWPBVP

Algorithm 1. Iterated Shooting Procedure.

```

initialize background fields on the compactified grid  $x$ 
initialize  $\delta\phi(x)$  to 0
initialize  $\delta\psi_R(x)$  and  $\delta\psi_I(x)$  to 0
while  $\delta N_\infty \gg 0$  do
  choose  $\beta^2$ 
  while solution non-convergent do
    hold  $\delta\phi(x)$  fixed
    shoot for  $\delta\psi_R(x)$  and  $\delta\psi_I(x)$ 
    fit tail to  $\delta\psi_R(x)$  and  $\delta\psi_I(x)$ 
    integrate  $\delta\nu(x)$ ,  $\delta\mu(x)$  and  $\delta N$  to
    asymptotic region

    hold  $\delta\psi_R(x)$  and  $\delta\psi_I$  fixed
    shoot for  $\delta\phi(x)$ 
    fit tail to  $\delta\phi(x)$ 
    integrate  $\delta\nu(x)$ ,  $\delta\mu(x)$  and  $\delta N$  to
    asymptotic region
  end while
end while

```

[30]. If the initial guess is sufficiently close to the true solution, the solver converges quickly, resulting in a solution which is accurate to within tolerance (typically 10^{-12} or better). By slowly adjusting the central amplitude, $\psi(0)$, of the stationary solution and using the previous solution to the perturbative equations as an initial guess, we can use the process of continuation to investigate the development of the mode throughout a branch of a family. [31].

As discussed in Sec. V, we only perform 2 or 3 evolutions per region to assess dynamical stability. In contrast, the process of continuation gives a much more comprehensive view of the mode structure within a region. By repeating this procedure on every branch and near every extremal point of M_∞ (including discontinuities), we can achieve an accurate picture of the mode structure of the family under investigation.

Note also that, due to the presence of asymptotic shells of matter which are present in some of these solutions, traditional shooting techniques may fail to adequately resolve the perturbed boson fields. The inability of double precision shooting to provide an adequate initial guess to the TWPBVPC based solver may be resolved, to some degree, through the use of extended precision integrators or through the use of our multiprecision shooting method [26]. Even then, we find that perturbative solutions in the presence of an asymptotic shell are quite difficult to find without the aid of continuation.

B. Convergence

As with the dynamical evolutions, we verify the convergence of our perturbative solutions via an independent residual convergence test. In this case, as in [26], care must be taken when computing these residuals due to the method by which TWPBVPC determines solutions. By default,

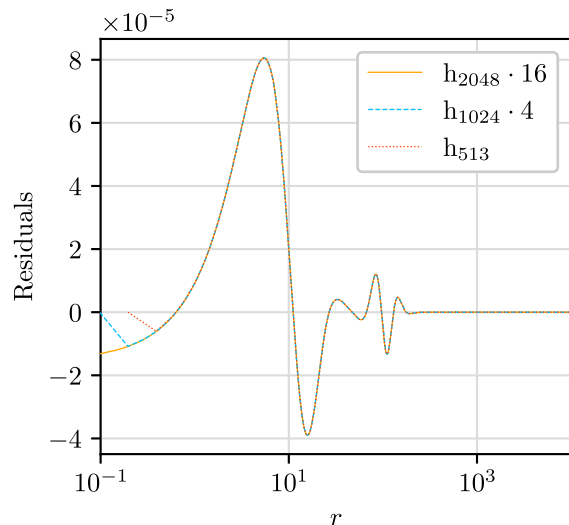


FIG. 6. Convergence of independent residuals for $\delta\lambda$ from family p_1 for a stable mode corresponding to $\psi(0) = 0.030$ and $\beta^2 \approx 3.21 \times 10^{-6}$. Here we plot the scaled residuals of the metric function evaluated on grids of 2049, 1025 and 513 points using a second order finite difference scheme for the independent residual evaluator. With the scaling given in the figure, overlap of the curves implies second order convergence.

TWPBVPC attempts to minimize solution error with a deferred error correction scheme that uses a combination of high order discretizations and allocation of additional grid points in the vicinity of poorly resolved features. Although these properties are invaluable for producing high quality solutions, they serve to increase the effective resolution and convergence order of a solution, making independent residual convergence difficult to verify. Consequently, Fig. 6 demonstrates the convergence of our collocation code with deferred error correction disabled.

VII. RESULTS

Section VII A presents the results of our dynamic simulations and summarizes the regions of stability found for the families of Table I. Section VII B summarizes the results of our perturbation theory analysis for families p_1 and p_2 . We derive a more complete picture of the modal structure for these families and provide important insight into the stability of other families of initial data. Finally, Sec. VII C compares the results from dynamical simulations and perturbation theory for family p_1 , demonstrating the broad equivalence of the two methods.

A. Dynamical simulations

Using slightly perturbed stationary solutions as initial data, 2 or 3 long time simulations for each region of each family in Table I were performed and the growth of perturbations in N , $\Psi\Psi^*$, Φ_M , a , and α were monitored. Simulations exhibiting collapse, dispersal or nonstationary

remnants were deemed unstable. Conversely, those showing oscillation about the stationary solutions with an oscillation magnitude set by the size of the initial perturbation were deemed stable. Again, we assume that the stability properties of all configurations in a given region are the same but perform a minimal validation of this assumption by performing at least 2-3 simulations per region.

In the interest of minimizing errors originating from our use of a dissipative second order code, these representative simulations were performed only near the centers of regions, fairly distant in parameter space from turning points of the mass and from branch jumps. In the case of regions with asymptotic shells, we concentrated our simulation efforts on areas where the d-stars were reasonably compact. In doing so, it was possible to uniformly excite modes and ensure that the light-crossing times for the compact objects were much less than the simulation time.

Figures 7–15 are composite plots showing both the asymptotic mass, M_∞ , and maximum compactness, C_{\max} as a function of boson star central amplitude for the families listed in Table I. Regions highlighted in gray are stable under small radial perturbations while regions outside the gray shading are unstable. The data points plotted here are drawn from our calculations of stationary solutions, not the much more sparsely sampled dynamical simulations. As noted above, the stability of each region was determined using far fewer simulations than there are points on the graph.

Special attention should be paid to Fig. 7 which shows the asymptotic mass, maximum compactness and regions of stability for the case of the mini-boson star. For mini-boson stars themselves, it is the region before the first

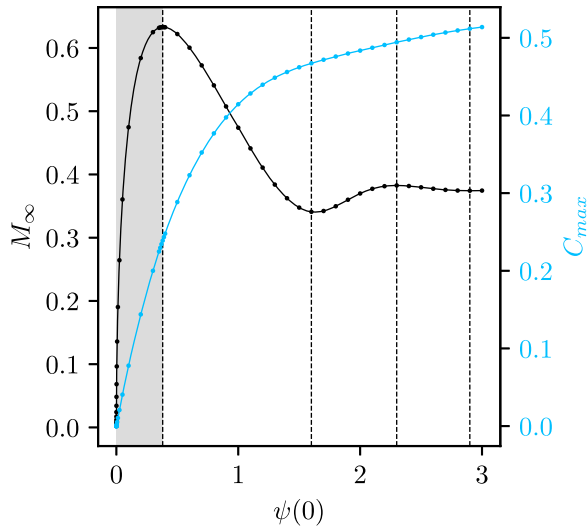


FIG. 7. Combined asymptotic mass and maximum compactness plot for the family of mini-boson stars (minimally coupled boson stars in the absence of a global monopole). The region of stability is denoted in gray. Dashed lines show turning points of the mass.

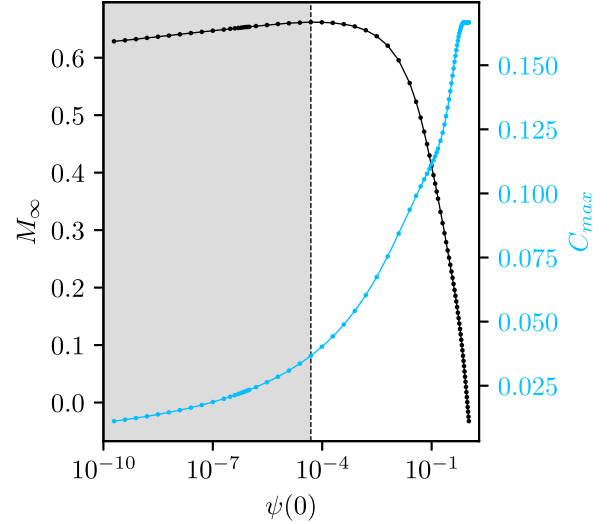


FIG. 8. Combined asymptotic mass and maximum compactness plot for family c ($\Delta^2 = 0.36$, $\lambda_G = 1.000$, $\xi_B = 0$, $\xi_G = 0$). The region of stability is denoted in gray. Dashed lines show turning points of the mass.

turning point in the mass that is stable [18,19]. In all d-stars investigated, the stable region, when it exists, corresponds to the region immediately before the first turning point on the final branch (where $\psi(0)$ assumes its largest values). Since we have previously shown that this final branch has no shells of bosonic matter far from the origin [26], we find that, for all families of d-stars so far investigated, regions of

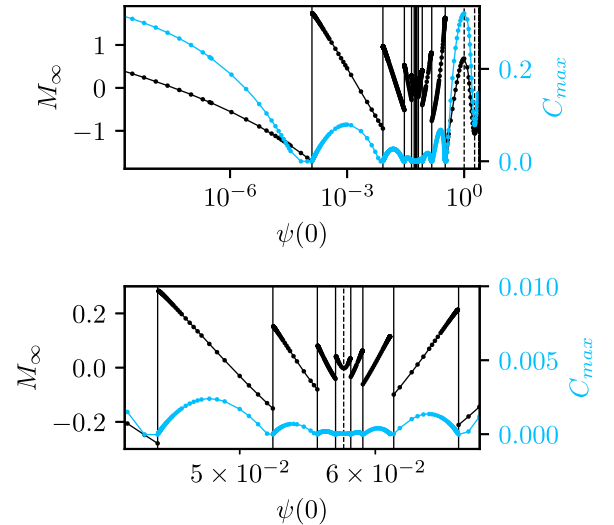


FIG. 9. Combined asymptotic mass and maximum compactness plot for family d ($\Delta^2 = 0.81$, $\lambda_G = 0.010$, $\xi_B = 0$, $\xi_G = 0$). No region of stability is found. Dashed vertical lines show turning points of the mass while solid vertical lines denote boundaries of solution branches. Here and in the next two plots the bottom panel shows a zoomed-in view of a portion of the data in the top panel.

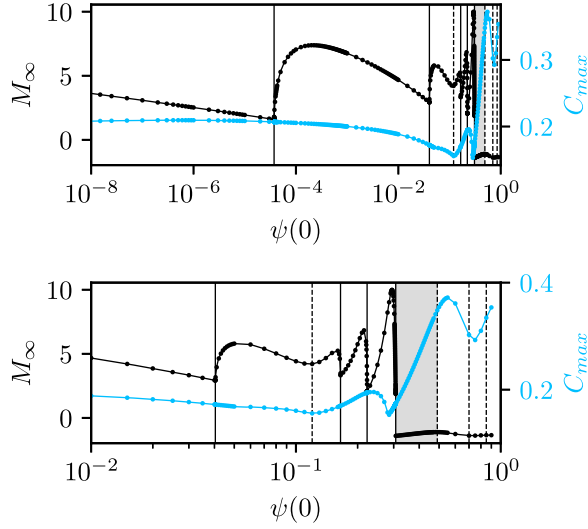


FIG. 10. Combined asymptotic mass and maximum compactness plot for family e ($\Delta^2 = 0.25$, $\lambda_G = 0.001$, $\xi_B = 3$, $\xi_G = 3$). The region of stability is shown in gray. Dashed vertical lines show turning points of the mass while solid vertical lines denote boundaries of solution branches.

stability are confined to boson-starlike branches without asymptotic shells.

B. Linear perturbation theory

In performing our perturbation theory analysis, we have restricted our investigation of d-stars to two minimally coupled families of solutions designated as p_1 and p_2 in Table I. These families were chosen for two primary reasons. First, they have relatively simple branching

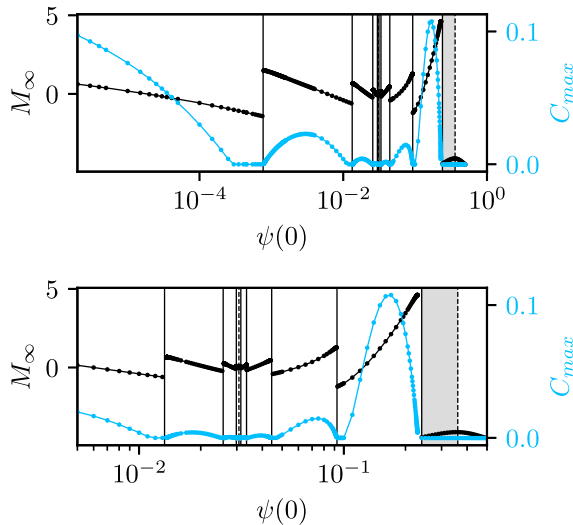


FIG. 11. Combined asymptotic mass and maximum compactness plot for family f ($\Delta^2 = 0.49$, $\lambda_G = 0.010$, $\xi_B = 5$, $\xi_G = 0$). The region of stability is shown in gray. Dashed vertical lines show turning points of the mass while solid vertical lines denote boundaries of solution branches.

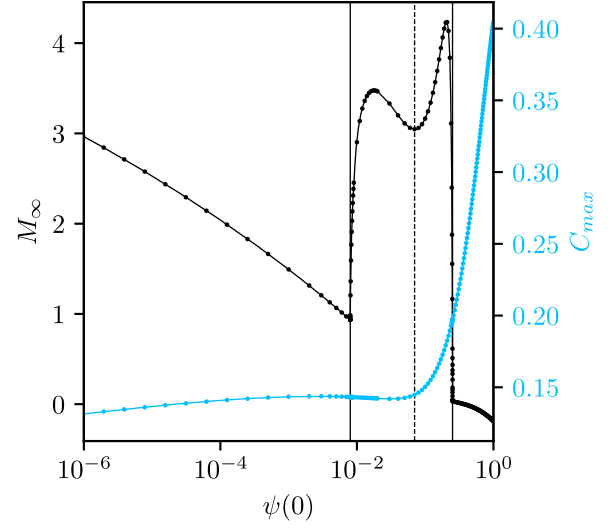


FIG. 12. Combined asymptotic mass and maximum compactness plot for family g ($\Delta^2 = 0.09$, $\lambda_G = 0.010$, $\xi_B = 0$, $\xi_G = 5$). No region of stability is found. Dashed vertical lines show turning points of the mass while solid vertical lines denote boundaries of solution branches.

structures (shown in Figs. 14 and 15) and this simplifies the perturbation analysis. Second, the two families are very close to one another in parameter space, yet have different numbers of solution branches. Correspondingly, their analysis yields clues as to how the modal structure changes as we vary parameters other than the family parameter, $\psi(0)$. For comparison purposes, we also include the results of perturbation theory applied to the case of minimally coupled mini-boson stars.

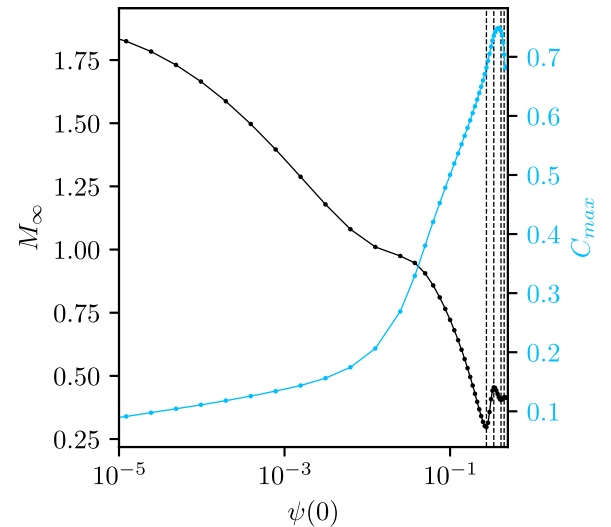


FIG. 13. Combined asymptotic mass and maximum compactness plot for family h ($\Delta^2 = 0.08$, $\lambda_G = 0.10$, $\xi_B = -4$, $\xi_G = 5$). No region of stability is found. Dashed vertical lines show turning points of the mass.

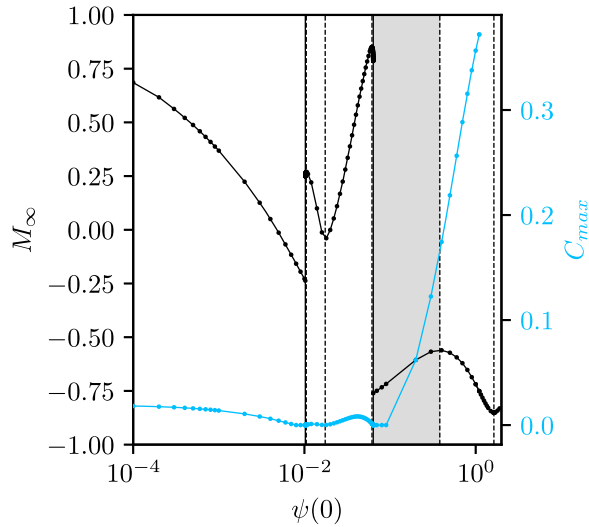


FIG. 14. Combined asymptotic mass and maximum compactness plot for family p_1 ($\Delta^2 = 0.09$, $\lambda_G = 0.04$, $\xi_B = 0$, $\xi_G = 0$). The region of stability is shown in gray. Dashed vertical lines show turning points of the mass while solid vertical lines denote boundaries of solution branches.

Plots displaying the modal structure for families p_1 and p_2 as well as for mini-boson stars are shown in Figs. 16–20, which plot eigenvalues, β^2 , as a function of the boson star central amplitude, $\psi(0)$. Stable regions have only modes with $\beta^2 > 0$ while unstable regions have modes both with $\beta^2 > 0$ and $\beta^2 < 0$. Note that the complete spectral structures are not shown. Rather, only the first few modes (the least stable) are displayed in each case.

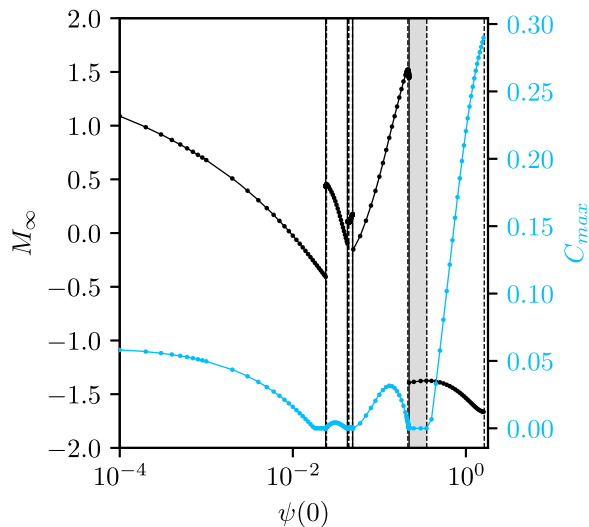


FIG. 15. Combined asymptotic mass and maximum compactness plot for family p_2 ($\Delta^2 = 0.25$, $\lambda_G = 0.04$, $\xi_B = 0$, $\xi_G = 0$). The region of stability is shown in gray. Dashed vertical lines show turning points of the mass while solid vertical lines denote boundaries of solution branches.

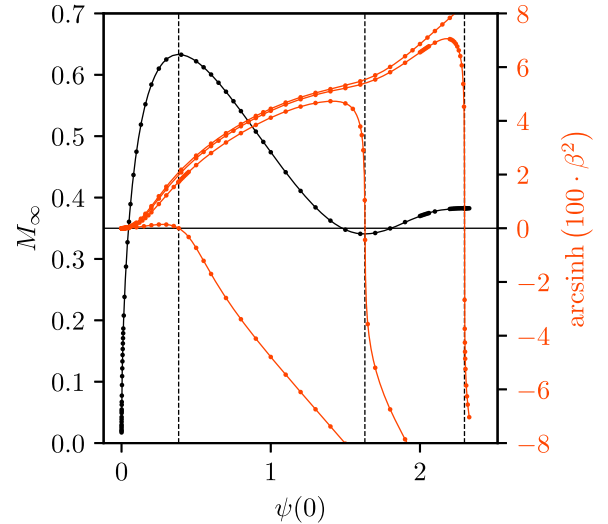


FIG. 16. Eigenvalues for the family of mini-boson stars. The modal structure shown here contrasts with behavior presented in Figs. 17–19 for minimally coupled d-stars. Note that at each turning point of the mass (vertical black dashed lines), a stable mode transitions to unstable. Here, and in subsequent plots, eigenvalues, β^2 , are shown as functions of $\sinh(\lambda\beta^2)$ to better display the overall modal structure: the magnitude of β^2 varies greatly so λ is chosen on a plot-by-plot basis to more clearly show the overall behavior of the eigenvalues.

In Figs. 17–20 we follow the convention of the previous sections and display the locations of branch transitions (corresponding to discontinuities in the mass and Noether charge) as black vertical lines while extrema of the mass are given as black dashed vertical lines. We observe that stability transitions within a branch occur at these extremal points as predicted by catastrophe theory [19,29].

Near the branch transitions, the eigenvalues of many modes appear to become degenerate, and neither our collocation or evolutionary codes are capable of investigating these regions in much detail. What is obvious, however, is that there is a well resolved unstable mode which persists across all but the final branch of families p_1 and p_2 . The presence of this unstable mode indicates that stable solutions exist only on the final branch, in perfect agreement with our dynamical simulations.

The lack of resolution resulting from the eigenvalue degeneracies in the vicinity of the branch transitions somewhat complicates the interpretation. We thus present a heuristic argument to build up a generic picture of the mode transitions. Recall from [26] that each branch transition before the mass turning point corresponds to the formation of a bosonic shell at infinity. This shell then migrates inward as the family parameter, $\psi(0)$, is increased. Each branch transition after the mass extrema then corresponds to the disappearance of a bosonic shell after it migrates outward.

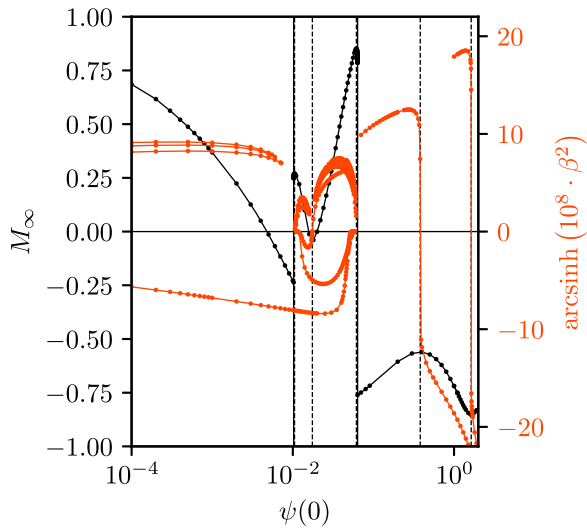


FIG. 17. Eigenvalues of family p_1 as a function of the boson star central amplitude, $\psi(0)$. Note the apparent discontinuities in the eigenvalues near branch transitions. In these regions, the eigenvalues become near-degenerate and our solutions are no longer convergent. Our observations, however, are consistent with the stable eigenvalues approaching $\beta^2 = 0$ at the branch transitions. Note also that there are an infinite number of stable modes in each region; here we have plotted only the first three.

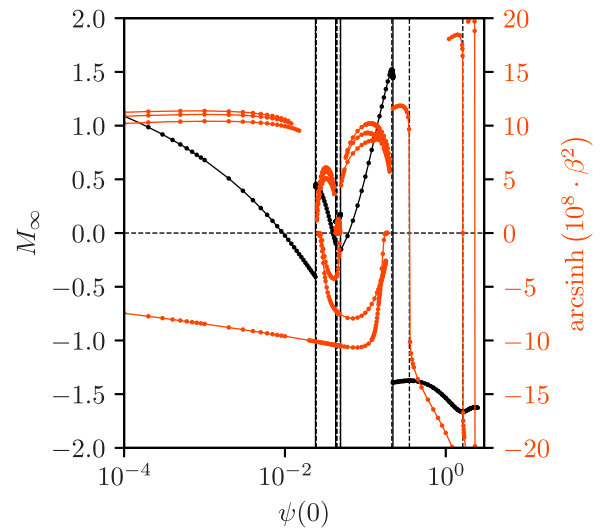


FIG. 19. Eigenvalues of family p_2 as a function of the boson star central amplitude, $\psi(0)$. The additional two branch transitions have split the second branch of family p_1 into three distinct regions (see Fig. 17). Note that the region after the final branch transition is qualitatively very similar to that of mini-boson stars as shown in Fig. 16. As for family p_1 , it can be seen that the central branches exhibit turning points in the mass corresponding to shells very far from the origin.

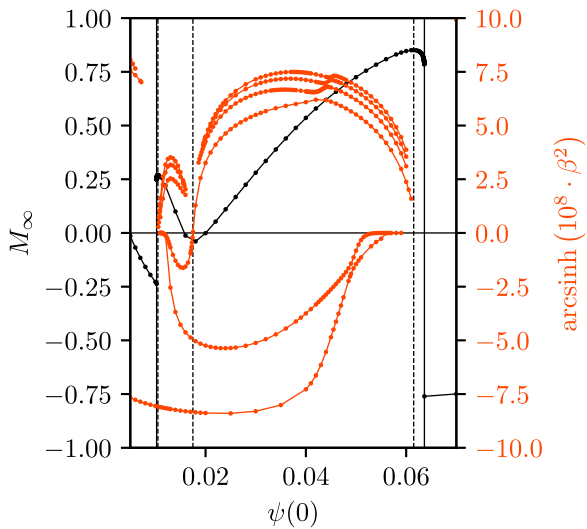


FIG. 18. A more detailed view of the central region of Fig. 17 for family p_1 . Interestingly, the central branch is composed of four regions (rather than two), with the first and last corresponding to shells very far from the origin. Unfortunately, the eigenvalue degeneracy prevents us from investigating these regions in detail, but it is regardless evident that the unstable modes persist through these regions (with the potential exception of the very last region where we were unable to resolve any perturbations).

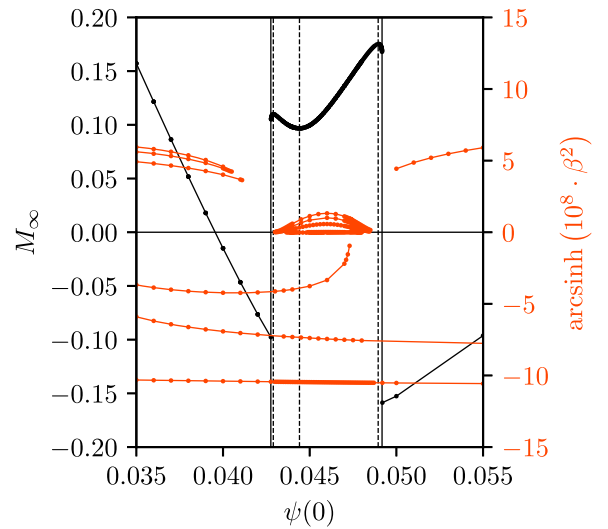


FIG. 20. Expanded view of Fig. 19 showcasing details that were poorly resolved in the original plot. Our simulation data is consistent with the eigenvalues of the poorly resolved modes approaching 0. As for family p_1 , it can be seen that the central branches exhibit turning points in the mass corresponding to shells very far from the origin. Unfortunately, the extreme length scales in these solutions, coupled with the eigenvalue degeneracy of the stable modes, prevents us from examining these regions in more detail.

In the case of families p_1 and p_2 , the first and final transitions can be identified with the appearance and disappearance of the first shell of matter. For family p_2 , the second and third transitions can likewise be identified with the appearance and disappearance of a second shell of matter. As noted above, family p_1 is very close to developing additional branch transitions similarly to family p_2 . For a marginally larger value of Δ^2 , family p_1 would have a degenerate transition corresponding to a shell of matter which appears suddenly at infinity and then immediately vanishes as the family parameter, $\psi(0)$, is increased. We can, in fact, see evidence of this behavior in Fig. 17 and idealized in Fig. 21 where the eigenvalues of the stable modes dip down toward 0 near the mass extrema.

This degenerate transition would split the transitioning mode into a stable and unstable region as shown in Fig. 22. As Δ^2 is increased further, the degeneracy is resolved, and we gain a new unstable mode corresponding to the new shell of matter as shown in Fig. 23. Given that there is still a mass extrema between the branch transitions, we will additionally have a new transitioning mode which changes from stable to unstable in accordance to catastrophe theory [19,29]. The final picture is then a series of stable eigenvalues between each branch transition joined via unstable modes in the manner depicted in Fig. 23.

C. Comparison of methods

Using the method of Sec. VII A, we extract the eigenvalues of the most unstable modes of the dynamical simulations for family p_1 and plot them against the results

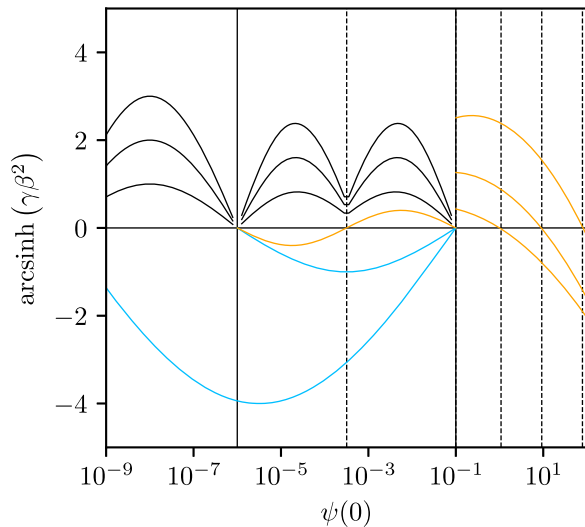


FIG. 21. Idealized plot of eigenvalues highlighting the underlying structure of family p_1 . Here we plot stable modes in black, unstable modes in blue and modes which undergo a stability transition within a branch in orange. Note in particular how in a family “close” to developing an additional branch transition, the eigenvalues “near” where the transition would develop become increasingly degenerate.

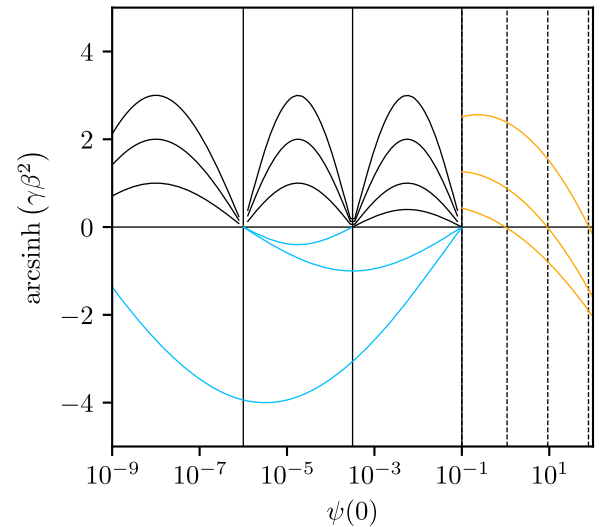


FIG. 22. Idealized plot of eigenvalues in the case of a degenerate branch transition. The transitioning mode has been split into a stable and unstable branch. As before, we plot stable modes in black, unstable modes in blue and modes which undergo a stability transition within a branch in orange.

predicted by perturbation theory in the previous section. In Fig. 24, eigenvalues from individual dynamical simulations are shown as blue circles while the eigenvalues from perturbation theory are shown in red.

Examining Fig. 24, we can see that the perturbation theory and the dynamical simulation are in agreement for the majority of the parameter space. An interesting issue, however, arises just before the final branch. In this region, the dynamical simulations suggest the existence of a stable

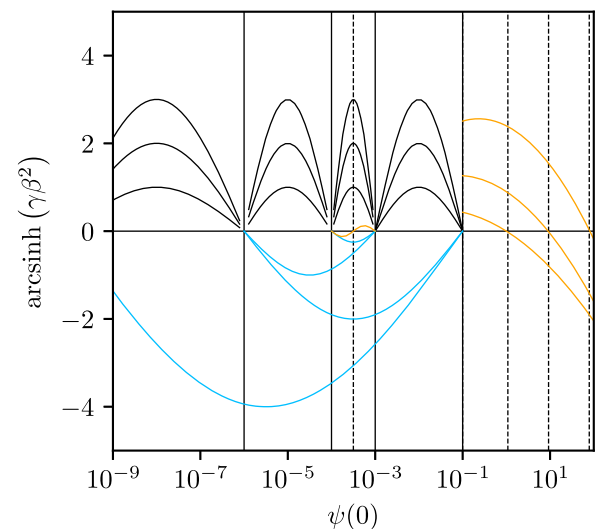


FIG. 23. Idealized plot of eigenvalues highlighting the underlying structure of family p_2 . As Δ^2 is increased further relative to p_1 , the degeneracy of Fig. 22 is resolved, and we gain a new branch of stable and unstable modes corresponding to the new shell of matter.

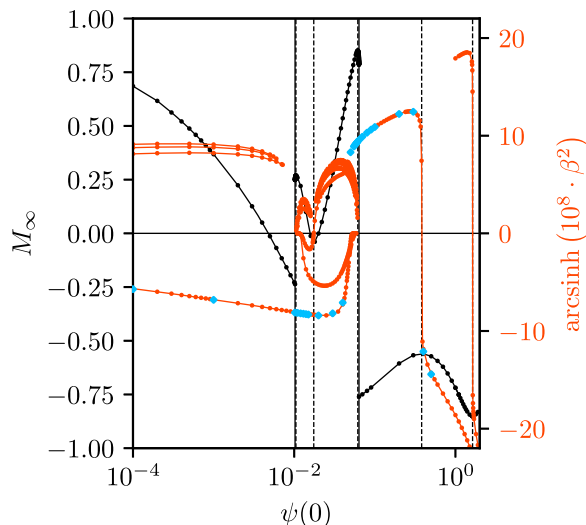


FIG. 24. Mass and mode structure for family p_1 . The asymptotic mass and eigenvalues measured via perturbation theory are shown in black and red as in Fig. 17. Eigenvalues measured directly from dynamical simulation are shown as blue diamonds. In the second branch, the blue diamonds indicating the existence of an oscillatory mode with $\beta^2 > 0$ do not correspond to any perturbative mode that we were able to identify.

oscillatory mode and the absence of the unstable mode found through perturbation theory.

This discrepancy is likely the result of two confounding factors. The first is that, in the region under consideration, the growth rate of the modes is extremely small ($|\beta^2| \lesssim 1 \times 10^{-8}$) so that the presence of an excited oscillatory mode could easily overwhelm the signal. If we were to integrate these solutions for a sufficiently long period of time, it seems likely that it would be possible to resolve the unstable eigenvalues. Unfortunately, the limited nature of our second order finite-difference based dynamical code makes maintaining temporal coherence for sufficiently long periods of time impractical. The second factor is that the oscillatory modes observed in this region are not purely oscillatory and instead decay slightly with time. As shown in Appendix B, however, the Hermitian character of this system requires that perturbations are either purely oscillatory or exponential in character. It seems likely that the oscillatory signals in these regions correspond to perturbations qualitatively close to those on the final branch which only nearly satisfy (B13)–(B18).

In addition to comparing the eigenvalues β^2 , it is possible to compare the profiles of the perturbations directly. Recall that for perturbations near the stationary solutions [for a given stationary field $f(t, r)$] we have

$$f(t, r) = f_0(r) + \delta f(r)e^{-\beta t}, \quad (51)$$

$$\partial_t f \propto \delta f. \quad (52)$$

As such, we may find an approximation to the Noether charge perturbation by taking the time derivative of the Noether charge. Doing so for families p_1 and p_2 , we find quite good agreement even for solutions with fairly distant bosonic shells.

VIII. SUMMARY

We have addressed the question of boson d-star stability and suitability as black hole mimickers proposed by Marunovic and Murkovic in [5]. Through simulations of a diverse families of initial data, we have demonstrated that regions of stability, where they exist, are confined to the boson-starlike final branch of a given family in both the minimally coupled and nonminimally coupled case.

We have verified this result in the case of minimally coupled families through a fairly comprehensive mode analysis of two families of initial data (p_1 and p_2) which are close to one another in phase space. This analysis supports the results of our dynamical simulations with both perturbation theory and direct simulation being in broad agreement. The only exception to this is in regions where the magnitude of the unstable eigenvalues are small. Our evolutionary code is ill suited to investigate these regions.

We observed how the number of branches and asymptotic shells change as the solid angle deficit, Δ^2 , is changed between these two families. By analysing the differences in mode structure between families p_1 and p_2 we propose a mechanism by which the mode structure changes in response to the appearance or disappearance of an asymptotic shell of bosonic matter.

Overall, our results are consistent with the interpretation that the highly compact solutions discovered in [5] are unstable. As a result, these solutions are likely poor candidates for astrophysically relevant compact objects. Finally, we observe that the novel solutions with shells of bosonic matter far from the origin discovered in [26] are likewise unstable.

ACKNOWLEDGMENTS

This research was supported by the Natural Sciences and Engineering Research Council of Canada (NSERC).

APPENDIX A: EQUATIONS OF MOTION

We start with the 3+1 equations in polar-areal coordinates and take $T_{\mu\nu}$ to be the combination $T_{\mu\nu} = T_{\mu\nu}^B + T_{\mu\nu}^G$ as defined in (4)–(5). In this gauge, the evolution of the metric function, a , is governed by

$$\partial_t a = \frac{T_{tr} a r}{2}, \quad (A1)$$

the Hamiltonian constraint is

$$\frac{2r\partial_r a}{a} = 1 - a^2 + \frac{a^2 r^2 T_{tt}}{a^2}, \quad (\text{A2})$$

and the slicing condition takes the form

$$2r\partial_r \alpha = \frac{2r\alpha\partial_r a}{a} + \left(\alpha T_{rr} - \frac{a^2 T_{tt}}{\alpha} \right) r^2 + 2\alpha(a^2 - 1). \quad (\text{A3})$$

Note that (A1) is redundant but provides a useful nontrivial consistency test for the system. In both the evolutionary and stationary cases, the Hamiltonian constraint and polar-areal slicing condition may be arranged to give explicit expressions for $\partial_r a$ and $\partial_r \alpha$, respectively. In this form, the Hamiltonian constraint is completely independent of α , and the constraints may be independently integrated. Moreover, since the constraints are first order in r , no boundary value solver is needed.

To simplify the resulting equations, we define the following quantities:

$$\zeta = \frac{1}{1 + \xi_B \phi_R^2 + \xi_B \phi_I^2 + \xi_G \Delta^2 \phi_M^2}, \quad (\text{A4})$$

$$\Lambda_r = (\phi_R \Phi_R + \phi_I \Phi_I) \xi_B + \xi_G \Delta^2 \phi_M \Phi_M, \quad (\text{A5})$$

$$\Lambda_t = (\phi_R \Pi_R + \phi_I \Pi_I) \xi_B + \xi_G \Delta^2 \phi_M \Pi_M, \quad (\text{A6})$$

$$\delta = 2 + 2\Lambda_r r \zeta. \quad (\text{A7})$$

Upon substitution of (A4)–(A7) into (A1)–(A3), we find the following equations for a and α :

$$\begin{aligned} \partial_t a = & \frac{2\xi_G \Delta^2 \zeta r \alpha (\phi_M \partial_r \Pi_M + \Pi_M \Phi_M)}{\delta} \\ & + \frac{2\xi_B \zeta r \alpha (\Pi_R \Phi_R + \Pi_I \Phi_I + \phi_R \partial_r \Pi_R + \phi_I \partial_r \Pi_I)}{\delta} \\ & - \frac{2\zeta r \alpha (\xi_G \Delta^2 \phi_M \Pi_M + \xi_B (\phi_R \Pi_R + \phi_I \Pi_I)) \partial_r a}{\delta a} \\ & + \frac{\zeta r \alpha (\Pi_R \Phi_R + \Pi_I \Phi_I + \Delta^2 \Pi_M \Phi_M + \Pi_P \Phi_P)}{\delta}, \end{aligned} \quad (\text{A8})$$

$$\begin{aligned} \frac{4\partial_r a}{r a^3} = & -\frac{2}{r^2} + \frac{2}{r^2 a^2} - \left[-2V - \frac{2\Delta^2 \phi_M^2}{r^2} \right. \\ & + \frac{1}{a^2} \left(-(\Phi_R^2 + \Phi_I^2 + \Pi_R^2 + \Pi_I^2 + \Phi_P^2 + \Pi_P^2 \right. \\ & + \Delta^2 [\Phi_M^2 + \Pi_M^2]) - 4(\phi_R \partial_r \Phi_R + \phi_I \partial_r \Phi_I \\ & + \Phi_R^2 + \Phi_I^2) \xi_B - 4(\phi_M \partial_r \Phi_M + \Phi_M^2) \Delta^2 \xi_G \\ & \left. \left. - \frac{8\Lambda_r}{r} + \frac{4\Lambda_t \partial_r a}{\alpha} + \frac{4\Lambda_r \partial_r a}{a^3} \right) \right] \zeta, \end{aligned} \quad (\text{A9})$$

$$\begin{aligned} \frac{\partial_r \alpha}{a^2 r} = & \frac{\alpha \partial_r a}{a^3 r} + \frac{\alpha}{r^2} - \frac{\alpha}{a^2 r^2} + \left[-\alpha V - \frac{\alpha \Delta^2 \phi_M^2}{r^2} \right. \\ & + \frac{(\phi_R \partial_r \Pi_R + \phi_I \partial_r \Pi_I) \xi_B + \Delta^2 \xi_G \phi_M \partial_r \Pi_M}{a} \\ & + \frac{\alpha \xi_B (-\phi_R \partial_r \Phi_R + \Pi_R^2 - \Phi_R^2)}{a^2} \\ & + \frac{\alpha \xi_B (-\phi_I \partial_r \Phi_I + \Pi_I^2 - \Phi_I^2)}{a^2} \\ & + \frac{\alpha \xi_G \Delta^2 (-\phi_M \partial_r \Phi_M + \Pi_M^2 - \Phi_M^2)}{a^2} \\ & \left. - \frac{4\Lambda_r \alpha}{a^2 r} - \frac{\Lambda_r}{a} \partial_r \left(\frac{\alpha}{a} \right) \right] \zeta. \end{aligned} \quad (\text{A10})$$

APPENDIX B: LINEAR PERTURBATION THEORY EQUATIONS

Following the decomposition of Sec. VI, we write the boson star field, Ψ , as

$$\Psi = e^{-i\omega t} (\psi_R + i\psi_I) = \phi_R + i\phi_I, \quad (\text{B1})$$

$$\phi_R(r, t) = \cos(\omega t) \psi_R(r, t) + \sin(\omega t) \psi_I(r, t), \quad (\text{B2})$$

$$\phi_I(r, t) = \cos(\omega t) \psi_I(r, t) - \sin(\omega t) \psi_R(r, t), \quad (\text{B3})$$

and perturb about the stationary solutions $\mu_0(r)$, $\nu_0(r)$, $\psi_0(r)$ and $\phi_0(r)$:

$$\mu(r, t) = \mu_0(r) + \epsilon \delta \mu(r) e^{i\beta t}, \quad (\text{B4})$$

$$\nu(r, t) = \nu_0(r) + \epsilon \delta \nu(r) e^{i\beta t}, \quad (\text{B5})$$

$$\psi_R(r, t) = \psi_0(r) + \epsilon \delta \psi_R(r) e^{i\beta t}, \quad (\text{B6})$$

$$\psi_I(r, t) = \frac{\epsilon}{i\beta} \delta \psi_I(r) e^{i\beta t}, \quad (\text{B7})$$

$$\phi_M(r, t) = \phi_0(r) + \epsilon \delta \phi(r) e^{i\beta t}. \quad (\text{B8})$$

Expanding the equations of motion to first order in ϵ , we find a complicated set of equations for linearized non-minimally coupled perturbations. To reduce the complexity of these equations, we restrict ourselves to the minimally coupled case ($\xi_B = \xi_G = 0$) whereby the stationary solutions satisfy:

$$\begin{aligned} \partial_r \mu_0 = & \left(\left(\frac{\lambda_B \psi_0^4}{4} + \left(\frac{m^2}{2} + \frac{\omega^2}{2e^{\nu_0}} \right) \psi_0^2 \right. \right. \\ & \left. \left. + \frac{\lambda_G \Delta^4 (\phi_0^2 - 1)^2}{4} \right) e^{\mu_0} + \frac{\Delta^2 (\partial_r \phi_0)^2}{2} \right. \\ & \left. + \frac{(\partial_r \psi_0)^2}{2} \right) r + \frac{1 + (\Delta^2 \phi_0^2 - 1) e^{\mu_0}}{r}, \end{aligned} \quad (\text{B9})$$

$$\begin{aligned} \partial_r \nu_0 = & \left(\left(\frac{-\lambda_B \psi_0^4}{4} - \left(\frac{m^2}{2} - \frac{\omega^2}{2e^{\nu_0}} \right) \psi_0^2 \right. \right. \\ & \left. \left. - \frac{\lambda_G \Delta^4 (\phi_0^2 - 1)^2}{4} \right) e^{\mu_0} + \frac{\Delta^2 (\partial_r \phi_0)^2}{2} \right. \\ & \left. + \frac{(\partial_r \psi_0)^2}{2} \right) r - \frac{1 + (\Delta^2 \phi_0^2 - 1) e^{\mu_0}}{r}, \end{aligned} \quad (\text{B10})$$

$$\begin{aligned} \partial_r^2 \psi_0 = & \left(\lambda_B \psi_0^3 + \left(m^2 - \frac{\omega^2}{e^{\nu_0}} \right) \psi_0 \right) e^{\mu_0} \\ & + \left(\frac{\partial_r \mu_0}{2} - \frac{\partial_r \nu_0}{2} - \frac{2}{r} \right) \partial_r \psi_0, \end{aligned} \quad (\text{B11})$$

$$\begin{aligned} \partial_r^2 \phi_0 = & \lambda_G \Delta^2 (\phi_0^3 - \phi_0) e^{\mu_0} + \frac{2\phi_0 e^{\mu_0}}{r^2} \\ & + \left(\frac{\partial_r \mu_0}{2} - \frac{\partial_r \nu_0}{2} - \frac{2}{r} \right) \partial_r \phi_0, \end{aligned} \quad (\text{B12})$$

and the equations for the perturbed quantities reduce to the following:

$$\partial_r \delta N = r^2 e^{\frac{1}{2}(\mu_0 - \nu_0)} \left(\frac{(\delta\mu - \delta\nu)\omega\psi_0^2}{4} + \left(\omega\delta\psi_R - \frac{\delta\psi_I}{2} \right) \psi_0 \right). \quad (\text{B13})$$

$$\begin{aligned} \partial_r \delta\mu = & \left(\left(\lambda_G \Delta^4 (\phi_0^3 - \phi_0) + \frac{2\Delta^2 \phi_0}{r^2} \right) \delta\phi \right. \\ & + \left(\frac{\lambda_B \psi_0^4}{4} + \left(\frac{m^2}{2} + \frac{\omega^2}{2e^{\nu_0}} \right) \psi_0^2 + \frac{\Delta^2 \phi_0^2 - 1}{r^2} \right. \\ & \left. + \frac{\lambda_G \Delta^4 (\phi_0^2 - 1)^2}{4} \right) \delta\mu + \lambda_B \psi_0^3 \delta\psi_R - \frac{\omega^2 \psi_0^2 \delta\nu}{2e^{\nu_0}} \\ & + \left(\left(m^2 + \frac{\omega^2}{e^{\nu_0}} \right) \delta\psi_R - \frac{\omega\delta\psi_I}{e^{\nu_0}} \right) \psi_0 e^{\mu_0} r \\ & + r\Delta^2 (\partial_r \phi_0) (\partial_r \delta\phi) + r(\partial_r \psi_0) (\partial_r \delta\psi_R), \end{aligned} \quad (\text{B14})$$

$$\begin{aligned} \partial_r \delta\nu = & \left(\left(2\lambda_G \Delta^4 (\phi_0 - \phi_0^3) - \frac{4\Delta^2 \phi_0}{r^2} \right) \delta\phi \right. \\ & - \frac{1}{2} \left(\lambda_G \Delta^4 (\phi_0^2 - 1)^2 + \frac{4(\Delta^2 \phi_0^2 - 1)}{r^2} \right. \\ & \left. + 2m^2 \psi_0^2 + \lambda_B \psi_0^4 \right) \delta\mu - 2(\lambda_B \psi_0^3 \\ & \left. + m^2 \psi_0) \delta\psi_R \right) e^{\mu_0} r + \partial_r \delta\mu, \end{aligned} \quad (\text{B15})$$

$$\begin{aligned} \partial_r^2 \delta\psi_R = & \frac{1}{2} \left(\partial_r \mu_0 - \partial_r \nu_0 - \frac{4}{r} \right) \partial_r \delta\psi_R \\ & + \frac{(\partial_r \delta\mu - \partial_r \delta\nu) \partial_r \psi_0}{2} + \left(\frac{(\delta\nu - \delta\mu)\omega^2 \psi_0}{e^{\nu_0}} \right. \\ & + (m^2 + 3\lambda_B \psi_0^2) \delta\psi_R + (m^2 \psi_0 + \lambda_B \psi_0^3) \delta\mu \\ & \left. + \frac{2\omega\delta\psi_I - (\omega^2 + \beta^2) \delta\psi_R}{e^{\nu_0}} \right) e^{\mu_0}, \end{aligned} \quad (\text{B16})$$

$$\begin{aligned} \partial_r^2 \delta\psi_I = & \frac{1}{2} \left(\partial_r \mu_0 - \partial_r \nu_0 - \frac{4}{r} \right) \partial_r \delta\psi_I \\ & + \left(\left(m^2 + \lambda_B \psi_0^2 - \frac{(\omega^2 + \beta^2)}{e^{\nu_0}} \right) \delta\psi_I \right. \\ & \left. + \frac{\omega\beta^2 (\delta\mu - \delta\nu) \psi_0}{2e^{\nu_0}} + \frac{2\omega\beta^2 \delta\psi_R}{e^{\nu_0}} \right) e^{\mu_0}, \end{aligned} \quad (\text{B17})$$

$$\begin{aligned} \partial_r^2 \delta\phi = & \frac{1}{2} \left(\partial_r \mu_0 - \partial_r \nu_0 - \frac{4}{r} \right) \partial_r \delta\phi \\ & + \left(\left(\lambda_G \Delta^2 (3\phi_0^2 - 1) + \frac{2}{r^2} \right) \delta\phi \right. \\ & + \left(\lambda_G \Delta^2 (\phi_0^3 - \phi_0) + \frac{2\phi_0}{r^2} \right) \delta\mu \\ & \left. - \frac{\beta^2 \delta\phi}{e^{\nu_0}} \right) e^{\mu_0} + \frac{(\partial_r \delta\mu - \partial_r \delta\nu) \partial_r \phi_0}{2}, \end{aligned} \quad (\text{B18})$$

Given that the deviations from the stationary solutions given by (B13)–(B18) involve perturbations of three dynamic fields (with the metric perturbations having no dynamic freedom of their own), it is not immediately obvious that the perturbations should be purely exponential or oscillatory in time. For example, one could imagine perturbations involving under or over damped oscillations corresponding to complex β^2 . Here, we follow the work of Jetzer [32], and demonstrate that a set of equations equivalent to (B13)–(B18) may be written in the following form,

$$L_{ij} \mathbf{f}_j = -\beta^2 e^{\mu_0 - \nu_0} G_{ij} \mathbf{f}_j, \quad (\text{B19})$$

where L_{ij} is a Hermitian differential operator, \mathbf{f}_j is the solution vector and G_{ij} is a diagonal matrix. It then follows that the eigenvalues of the above pulsation equation (for β^2) are purely real. As before we expand our fields about the stationary solutions, but do not yet enforce exponential time dependence:

$$\mu(t, r) = \mu_0(r) + \epsilon \delta\mu(t, r), \quad (\text{B20})$$

$$\nu(t, r) = \nu_0(r) + \epsilon \delta\nu(t, r), \quad (\text{B21})$$

$$\psi_R(t, r) = \psi_0(r) + \epsilon \delta\psi_R(t, r), \quad (\text{B22})$$

$$\psi_I(t, r) = \epsilon \psi_0(r) \delta\psi_I(t, r), \quad (\text{B23})$$

$$\phi(t, r) = \phi_0(r) + \epsilon \delta\phi(t, r). \quad (\text{B24})$$

Substituting these expressions into the equations of motion for the fields and metric and truncating to linear order in the perturbation, we find a coupled system of perturbation equations. In particular, the equation $G_{rt} = T_{rt}$ produces the following simple expression for $\delta\mu$:

$$\begin{aligned} \partial_t \delta\mu = & r(\Delta^2(\partial_t \delta\phi)(\partial_r \phi_0) - (\partial_r \delta\psi_I)\psi_0^2\omega \\ & + (\partial_r \psi_0)(\partial_t \psi_R)). \end{aligned} \quad (\text{B25})$$

With the substitution

$$\delta\psi_I = \partial_t \delta\tilde{\psi}_I, \quad (\text{B26})$$

(B25) becomes a total derivative with respect to time and may be integrated to give,

$$\begin{aligned} \delta\mu = & r(\Delta^2(\delta\phi)(\partial_r \phi_0) + (\delta\psi_R)(\partial_r \psi_0) \\ & - (\omega\psi_0^2)\partial_r \delta\tilde{\psi}_I). \end{aligned} \quad (\text{B27})$$

We may also obtain an expression for $\delta\nu$ by solving the perturbed $G_{tt} = T_{tt}$ equation for $\delta\nu$ and substituting the relevant expressions for $\delta\psi_I$, $\delta\mu$, $\partial_r^2 \psi_0$, $\partial_r^2 \phi_0$, $\partial_r \mu_0$, and $\partial_r \nu_0$:

$$\begin{aligned} \delta\nu = & -\frac{r e^{\nu_0} \lambda_G \Delta^4 (\phi_0^2 - 1)^2 \partial_r \delta\tilde{\psi}_I}{2\omega} - \frac{2\partial_r^2 \delta\tilde{\psi}_I}{\omega} \\ & + \Delta^2 \left(\delta\phi(\partial_r \phi_0) r - \frac{2\phi_0^2 e^{\nu_0} (\partial_r \delta\tilde{\psi}_I)}{r\omega} \right) \\ & + e^{\nu_0} \left(\frac{2}{r\omega} - \frac{(\lambda_B \psi_0^4 + 2m^2 \psi_0^2) r}{2\omega} \right) \partial_r \delta\tilde{\psi}_I \\ & - r\omega\psi_0^2 (\partial_r \delta\tilde{\psi}_I) + \left(r\partial_r \psi_0 + \frac{4}{\psi_0} \right) \delta\psi_R \\ & + 2 \left(\left(\frac{2\partial_r \psi_0}{\psi_0} + \frac{1}{r} \right) \partial_r \delta\tilde{\psi}_I + \partial_r^2 \delta\tilde{\psi}_I \right) \frac{e^{\nu_0}}{\omega e^{\mu_0}}. \end{aligned} \quad (\text{B28})$$

With the perturbed metric functions now defined solely in terms of the stationary solution and perturbed matter fields, we find expressions for $\partial_r^2 \delta\psi_R$, $\partial_r^3 \delta\tilde{\psi}_I$ and $\partial_r^2 \delta\phi$ through substitution. At this stage, the perturbation equations consist of three second order expression in $\mathbf{f}_j = (\delta\psi_R, \partial_r \delta\tilde{\psi}_I, \delta\phi)$ with all time derivatives appearing as second order expressions. Substituting:

$$\delta\tilde{\psi}_I(r, t) = \delta\tilde{\psi}_I(r) e^{i\beta t}, \quad (\text{B29})$$

$$\delta\psi_R(r, t) = \delta\psi_R(r) e^{i\beta t}, \quad (\text{B30})$$

$$\delta\phi(r, t) = \delta\phi(r) e^{i\beta t}, \quad (\text{B31})$$

we may write our coupled perturbation expressions as,

$$\tilde{L}_{ij} \mathbf{f}_j = -\beta^2 e^{\mu_0 - \nu_0} \mathbf{f}_j, \quad (\text{B32})$$

where \tilde{L}_{ij} is a second order, non-Hermitian operator of the following form:

$$\begin{bmatrix} \frac{\partial^2}{\partial r^2} + a_1 \frac{\partial}{\partial r} + b_1 & c_1 \frac{\partial}{\partial r} + d_1 & e_1 \\ c_2 \frac{\partial}{\partial r} + d_2 & \frac{\partial^2}{\partial r^2} + a_2 \frac{\partial}{\partial r} + b_2 & h_2 \\ e_3 & h_3 & \frac{\partial^2}{\partial r^2} + a_3 \frac{\partial}{\partial r} + b_3 \end{bmatrix}. \quad (\text{B33})$$

Here, all subscripted quantities should be understood to be functions of r . The goal is now to find a diagonal matrix, M_{ij} , such that $L_{ij} = M_{ik} \tilde{L}_{kj}$ is a Hermitian operator of the form

$$\begin{bmatrix} \frac{\partial}{\partial r} M_1 \frac{\partial}{\partial r} + B_1 & -\frac{\partial}{\partial r} C_1 + D_1 & E_1 \\ C_1 \frac{\partial}{\partial r} + D_1 & \frac{\partial}{\partial r} M_2 \frac{\partial}{\partial r} + B_2 & H_1 \\ E_1 & H_1 & \frac{\partial}{\partial r} M_3 \frac{\partial}{\partial r} + B_3 \end{bmatrix}, \quad (\text{B34})$$

and

$$M_{ij} = \begin{bmatrix} M_1 & 0 & 0 \\ 0 & M_2 & 0 \\ 0 & 0 & M_3 \end{bmatrix}. \quad (\text{B35})$$

Fortunately, this turns out to be a well-defined problem and the M_i 's and C_1 take the form:

$$M_1 = r^2 e^{\frac{1}{2}(\nu_0 - \mu_0)}, \quad (\text{B36})$$

$$M_2 = r^2 e^{\frac{3}{2}(\nu_0 - \mu_0)} \psi_0^2, \quad (\text{B37})$$

$$M_3 = r^2 \Delta^2 e^{\frac{1}{2}(\nu_0 - \mu_0)}, \quad (\text{B38})$$

$$C_1 = 2\omega r^2 \psi_0 e^{\frac{1}{2}(\nu_0 - \mu_0)}, \quad (\text{B39})$$

while the remaining terms are sufficiently cumbersome that it is not particularly enlightening to write them out explicitly. One could, of course, use the equations just derived to solve the perturbation problem rather than (B13)–(B18). Unfortunately, as is often the case with such matters, by the time we verified that the equations permitted only real eigenvalues, the previous formalism had already been adopted and investigated. Due to the significant reduction in complexity these equations represent, we would highly recommend future work to follow this approach rather than the more direct method we adopted.

- [1] J. A. Wheeler, Geons, *Phys. Rev.* **97**, 511 (1955).
- [2] D. J. Kaup, Klein–Gordon geon, *Phys. Rev.* **172**, 1331 (1968).
- [3] R. Ruffini and S. Bonazzola, Systems of self-gravitating particles in general relativity and the concept of an equation of state, *Phys. Rev.* **187**, 1767 (1969).
- [4] S. L. Liebling and C. Palenzuela, Dynamical boson stars, *Living Rev. Relativity* **26**, 1 (2023).
- [5] A. Marunović and M. Murković, A novel black hole mimicker: A boson star and a global monopole nonminimally coupled to gravity, *Classical Quantum Gravity* **31**, 045010 (2014).
- [6] J. Barranco and A. Bernal, Constraining scalar field properties with boson stars as black hole mimickers, *AIP Conf. Proc.* **1396**, 171 (2011).
- [7] D. F. Torres, S. Capozziello, and G. Lambiase, Supermassive boson star at the Galactic center?, *Phys. Rev. D* **62**, 104012 (2000).
- [8] Y.-F. Yuan, R. Narayan, and M. J. Rees, Constraining alternate models of black holes: Type I x-ray bursts on accreting fermion-fermion and boson-fermion stars, *Astrophys. J.* **606**, 1112 (2004).
- [9] C. Palenzuela, L. Lehner, and S. L. Liebling, Orbital dynamics of binary boson star systems, *Phys. Rev. D* **77**, 044036 (2008).
- [10] C. Palenzuela, I. Olabarrieta, L. Lehner, and S. L. Liebling, Head-on collisions of boson stars, *Phys. Rev. D* **75**, 064005 (2007).
- [11] E. W. Mielke and F. E. Schunck, Boson stars: Early history and recent prospects, in *Recent Developments in Theoretical and Experimental General Relativity, Gravitation, and Relativistic Field Theories* (World Scientific Publishing Company, Singapore, 1999), Vol. 1, p. 1607.
- [12] F. E. Schunck and D. F. Torres, Boson stars with generic self-interactions, *Int. J. Mod. Phys. D* **9**, 601 (2000).
- [13] U. Nucamendi, M. Salgado, and D. Sudarsky, Alternative approach to the galactic dark matter problem, *Phys. Rev. D* **63**, 125016 (2001).
- [14] L. A. Urena-Lopez and A. Bernal, Bosonic gas as a galactic dark matter halo, *Phys. Rev. D* **82**, 123535 (2010).
- [15] T. Rindler-Daller and P. R. Shapiro, Angular momentum and vortex formation in Bose–Einstein-condensed cold dark matter haloes, *Mon. Not. R. Astron. Soc.* **422**, 135 (2012).
- [16] M. Y. Khlopov, B. A. Malomed, and Y. B. Zeldovich, Gravitational instability of scalar fields and formation of primordial black holes, *Mon. Not. R. Astron. Soc.* **215**, 575 (1985).
- [17] T. Lee and Y. Pang, Stability of mini-boson stars, *Nucl. Phys.* **B315**, 477 (1989).
- [18] M. Gleiser and R. Watkins, Gravitational stability of scalar matter, *Nucl. Phys.* **B319**, 733 (1989).
- [19] F. V. Kusmartsev, E. W. Mielke, and F. E. Schunck, Gravitational stability of boson stars, *Phys. Rev. D* **43**, 3895 (1991).
- [20] M. Colpi, S. L. Shapiro, and I. Wasserman, Boson stars: Gravitational equilibria of self-interacting scalar fields, *Phys. Rev. Lett.* **57**, 2485 (1986).
- [21] P. Amaro-Seoane, J. Barranco, A. Bernal, and L. Rezzolla, Constraining scalar fields with stellar kinematics and collisional dark matter, *J. Cosmol. Astropart. Phys.* **11** (2010) 002.
- [22] M. Barriola and A. Vilenkin, Gravitational field of a global monopole, *Phys. Rev. Lett.* **63**, 341 (1989).
- [23] X. Shi and X. Li, The gravitational field of a global monopole, *Classical Quantum Gravity* **8**, 761 (1991).
- [24] A. Vilenkin and E. P. S. Shellard, *Cosmic Strings and Other Topological Defects* (Cambridge University Press, Cambridge, England, 2000).
- [25] U. Nucamendi and D. Sudarsky, Quasi-asymptotically flat spacetimes and their ADM mass, *Classical Quantum Gravity* **14**, 1309 (1997).
- [26] G. Reid and M. W. Choptuik, Nonminimally coupled topological-defect boson stars: Static solutions, *Phys. Rev. D* **93**, 044022 (2016).
- [27] X.-z. Li and X.-h. Zhai, Fermion stars with a global monopole, *Phys. Lett. B* **364**, 212 (1995).
- [28] X.-z. Li, X.-h. Zhai, and G. Chen, Boson d-stars, *Astropart. Phys.* **13**, 245 (2000).
- [29] B. Kleihaus, J. Kunz, and S. Schneider, Stable phases of boson stars, *Phys. Rev. D* **85**, 024045 (2012).
- [30] F. Mazzia, J. R. Cash, and K. Soetaert, Solving boundary value problems in the open source software R: Package bvpSolve, *Opusc. Math.* **34**, 387 (2014).
- [31] From a technical perspective, it is worth noting how the β^2 eigenvalue is incorporated in TWPBVPC. Following [33], we implemented the β^2 eigenvalue as an additional field satisfying the trivial equation $\partial_x(\beta^2(x)) = 0$.
- [32] P. Jetzer, Boson stars, *Phys. Rep.* **220**, 163 (1992).
- [33] A. Marunovic (personal communication).